

# Non-isothermal CO<sub>2</sub> electrolysis enables simultaneous enhanced electrochemical and anti-precipitation performance

Received: 18 February 2025

Jieyang Li, Huanlei Zhang, Changhao Luo, Dongbo Cheng, Wanping Xu & Meng Lin  

Accepted: 30 April 2025

Published online: 06 May 2025

 Check for updates

Electrochemical conversion of CO<sub>2</sub> into fuels represents an important pathway for addressing the challenges of climate change and energy storage. However, large-scale applications remain hindered by the instability and inefficiency of CO<sub>2</sub> reduction systems, particularly under highly alkaline electrolytes and high current densities. One primary obstacle is the cathodic salt precipitation, which hinders mass transfer and blocks active sites limiting the lifespan of these systems. Here, we present a non-isothermal strategy that leverages a thermal gradient across the membrane electrode assembly to enhance electrochemical performance and suppress salt precipitation. By maintaining a cooler cathode and warmer anode, we exploit the Soret effect to drive cations away from the cathode, mitigating salting-out while boosting anodic activity and cathodic CO<sub>2</sub> solubility. The non-isothermal case has demonstrated over 200 h of stable operation at 100 mA cm<sup>-2</sup> under highly alkaline conditions, outperforming conventional isothermal systems. Techno-economic analysis reveals reductions in CO<sub>2</sub>-to-CO production costs, supporting the scalability of this strategy. These findings enable the practical deployment of stable, high-efficiency CO<sub>2</sub> electrolysis systems.

Converting intermittent renewable electricity and CO<sub>2</sub> into storable fuels at scale is critical for advancing renewable energy storage and achieving effective CO<sub>2</sub> mitigation on an industrial level<sup>1-3</sup>. Ambient temperature electrochemical CO<sub>2</sub> reduction reactions (CO<sub>2</sub>RRs) are of particular interest due to their ability to produce a diverse range of products via dedicated electrolyzer and catalyst designs. Recent advancements in the development of electrocatalysts and electrolyzer architectures for CO<sub>2</sub>RRs lead to enhanced catalytical and CO<sub>2</sub> utilization performances. However, the industrial deployment of CO<sub>2</sub>RR requires high operational current densities ( $\geq 100$  mA cm<sup>-2</sup>)<sup>4,5</sup> to minimize capital costs and ensure long-term operational stability, thereby reducing maintenance expenses<sup>6</sup>.

Typical exchange membrane electrode assembly (MEA)-based CO<sub>2</sub>R electrolyzers using alkaline electrolytes have favorable electrochemical performance in terms of activity and selectivity<sup>7,8</sup>. The lower overpotential observed under highly alkaline conditions facilitates

direct coupling with renewable energy sources, such as solar energy via photovoltaic cells<sup>9</sup>. However, despite advancements in electrocatalyst development and device architectures, sustaining long-term stability at elevated current densities remains a significant challenge, primarily due to cathodic salt precipitation in MEA-based reactors. Particularly, when highly alkaline electrolytes are utilized, the salt precipitation phenomenon<sup>10-14</sup> limits the system lifetime by blocking the MEA's pore and the channels<sup>15</sup>. In highly alkaline environments, particularly with KOH as the electrolyte, the abundance of hydroxide ions (OH<sup>-</sup>) generated by the cathodic CO<sub>2</sub>R readily reacts with excess CO<sub>2</sub> to form (bi)carbonate ions (CO<sub>3</sub><sup>2-</sup>/HCO<sub>3</sub><sup>-</sup>). Recent research has demonstrated that the type and concentration of cations can tune the catalytic performance by modifying the local electric field, buffering the interfacial pH, and stabilizing reaction intermediates<sup>16-18</sup>. However, the migration of cations (K<sup>+</sup>) from the anode accumulating in the cathode leads to the formation of bicarbonate salts (KHCO<sub>3</sub>/K<sub>2</sub>CO<sub>3</sub>),

which precipitate upon reaching supersaturation to block the pores and channels of the MEA and further suppress the catalytic performance. Various operational strategies primarily aiming to reduce  $[K^+]$ ,  $[CO_3^{2-}/HCO_3^-]$ , or  $[KHCO_3/K_2CO_3]$  concentrations in the cathode compartment have been employed to prevent salt formation. Common approaches include disassembling the MEA electrolyzer for flushing the cathodic flow channel with water or an activation solution, which, while effective, is discontinuous and disrupts operation<sup>8,19</sup>. Other methods, such as reducing anolyte concentration, altering cation identity, or using deionized water, aim to prevent cation accumulation at the cathode surface<sup>20</sup>. The dilute electrolyte can diminish salt precipitation to some extent, but this comes at the cost of reduced electrolyzer performance as a result of higher overpotential and lower conductivity of ions. Alternating voltage and pulsed electrolysis strategies have been proposed to maintain  $CO_3^{2-}$  concentrations below the threshold for precipitation by converting  $CO_3^{2-}$  to the anode at lower regeneration voltages<sup>21</sup>. Yet, these approaches introduce non-steady-state conditions, increasing the transport of carbon sources to the anode without participating in  $CO_2R$ , leading to electrolyte acidification and reduced  $CO_2$  utilization efficiency.

In this study, we introduce a non-isothermal operation approach, employing a cooler cathode and a warmer anode, to simultaneously enhance device efficiency and prevent salt precipitation. This is achieved by exploiting the Soret effect<sup>22,23</sup>, which drives the thermal diffusion of cations from the cathode to the anode. Additionally, this approach capitalizes on the increased electrochemical activity of the anodic oxygen evolution reaction (OER) at higher temperatures and the enhanced selectivity of the cathode due to increased  $CO_2$  solubility at lower temperatures<sup>24</sup>. Our experimental results reveal that a membrane electrode assembly-based  $CO_2$  reduction device for the non-isothermal cases showed long-term stability without salting-out under highly alkaline conditions at a current density of  $100\text{ mA cm}^{-2}$ . This non-isothermal operation strategy represents a significant advancement in the practical implementation of  $CO_2$  reduction technologies, ensuring long-term operational stability without compromising energy conversion efficiency. By overcoming one of the key limitations in current  $CO_2$  electrolysis systems, our approach paves the way for more sustainable and scalable industrial applications.

## Results

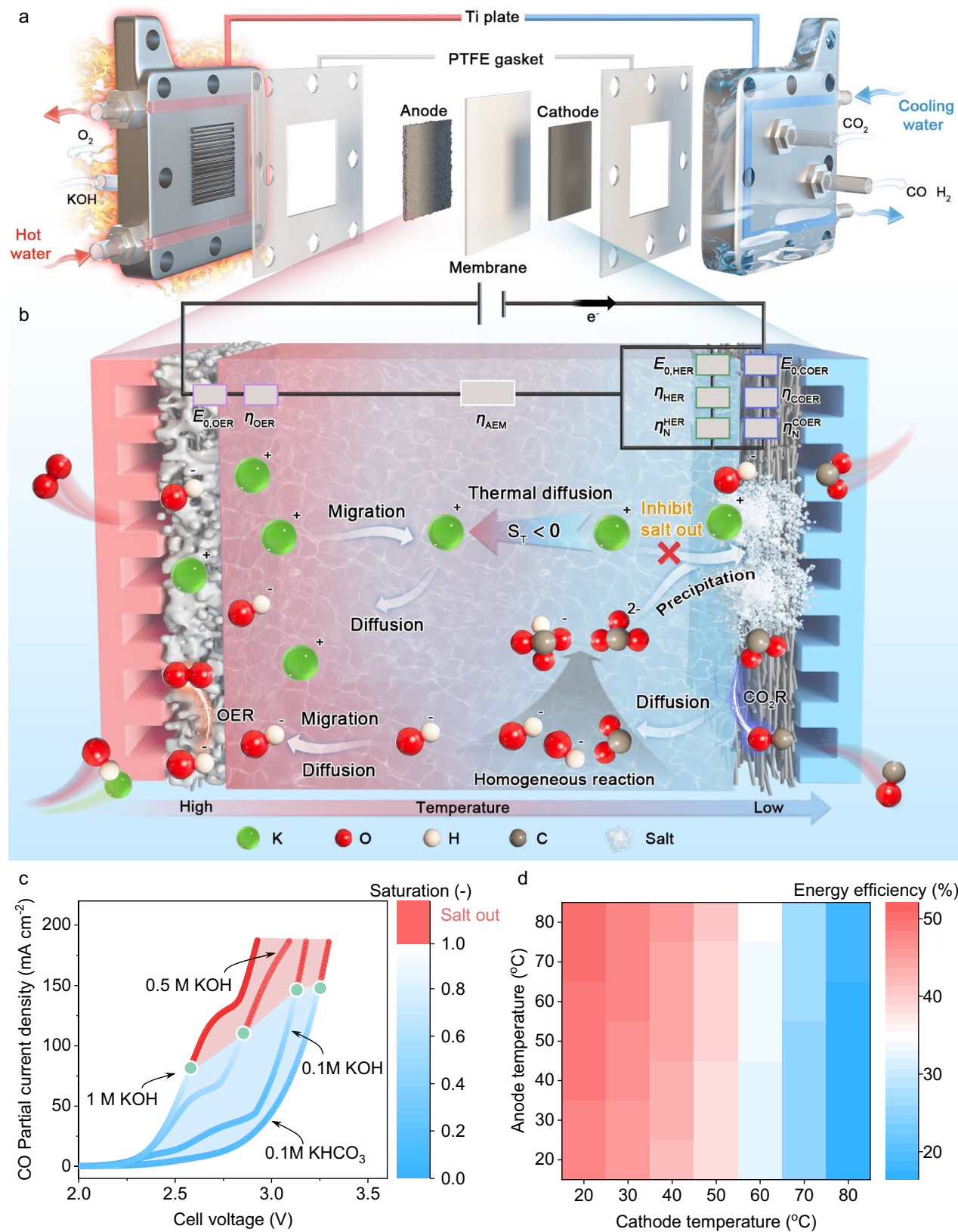
### Performance prediction of MEA-based $CO_2RR$

Here we demonstrate the effectiveness of the proposed non-isothermal operation strategy by operating the cathode at a lower temperature while the anode at a higher temperature for a  $CO_2R$  electrolyzer with individually optimized electrode reaction environments and a salting out free cathode (see Fig. 1a, b and Supplementary Figs. S1 and S2 for the non-isothermal strategy). A cooler cathode can benefit from the increased  $CO_2$  dissolution and suppressed hydrogen evolution reaction (HER), i.e., reduced concentration overpotential,  $\eta_{CO}$ , and increased Faradaic efficiency, and a warmer anode can benefit from higher catalytic activity at higher temperature, i.e., activation overpotential,  $\eta_{OER}$ . Moreover, the warmer membrane closer to the anode side also increases the conductivity of the membrane and hence reduces the ohmic overpotential, i.e.,  $\eta_{ohmic}$ . As the reduction reaction consumes  $H^+$  or generates  $OH^-$ , leading to a pH difference between the anode and the cathode. The Nernstian potential due to this pH difference can be accounted for by Eqs. S22 in the Supplementary information. Since the Nernstian potential is temperature-dependent, the temperature effect can also be quantified. The salt precipitation can be avoided by the temperature gradient induced Soret effect (Supplementary Discussion S1 and Fig. S3), pumping the cation from the cathode to the anode, which counteracts the migration-induced co-ion leakage (Fig. 1a), hence mitigating the salt precipitation. We theoretically predicted the electrochemical performance and the salt precipitation using a non-isothermal multi-physical model (details in

Supplementary Discussion S2, Tables S1–S5, and Figs. S4–S7) considering heat and mass transfer as well as the electrochemical and homogeneous reactions within a typical MEA-based electrolyzer. This minor  $K^+$  partial current, typically ~0.1% at a typical current density of  $200\text{ mA cm}^{-2}$ , 3.5 V<sup>25</sup> is the source for the formation of  $KHCO_3$  and  $K_2CO_3$  at the cathode side, which subsequently leads to salt precipitation<sup>15</sup>. The concentration of  $K^+$  at cathode in general has a higher concentration than the anode side, especially at high current density, since the  $K^+$  is the major cation at the cathode. That means, at high current density, the generated  $OH^-$  requires an increasing concentration of  $K^+$  to achieve electroneutrality outside the electrical double layer. This also means the concentration gradient is favorable for the back diffusion of  $K^+$  from cathode to anode. In sum, in the non-isothermal case, the diffusion due to concentration and temperature gradient can counteract the electrical field induced migration to avoid over-saturation of K-based salts. The  $IrO_2-Ti$  (Supplementary Method and Fig. S8) and Ag nano-particles (Ag-NPs) (Supplementary Method and Figs. S9 and S10) were considered as the cathode and anode electrocatalytic materials, respectively, utilizing various alkaline anolytes. Fig. 1c illustrates the polarization curves and the on-site current densities of salt precipitation (marked in green points) under different anode electrolytes (KOH,  $KHCO_3$ ), showing electrolytes with high alkalinity tend to have salt-out issues at lower current densities. Note that the term "salt" refers to the  $K_2CO_3$  at the cathode. For a specific cell voltage, the  $CO$  partial current densities are shifted to higher values with increasing anolyte alkalinity, suggesting a better electrochemical performance. Meanwhile, the onset of salting out cell voltage (green dots in Fig. 1c, when the local salt concentration reaches its saturation) was lowered at anolyte with high alkalinity, suggesting that a non-compromised device performance requires salting out free operation at high alkalinity. The reduced  $CO_2$  gas flow rate and increased relative humidity are observed to mitigate salt precipitation (see Supplementary Fig. S11). Figure 1d shows that performance enhancement can be achieved by implementing our non-isothermal strategy. Operating anode at  $80^\circ\text{C}$  and the cathode at  $20^\circ\text{C}$ , typical ambient temperature, lead to an energy efficiency of 50.6%, while the efficiency was only 47.5% in isothermal  $20^\circ\text{C}$  case and 17.9% in isothermal  $80^\circ\text{C}$  case, showing a relative 3.1% and 32.7% enhancement in performance, respectively.

### Non-isothermal $CO_2R$ concept

To experimentally validate the non-isothermal  $CO_2R$  concept proposed in this study, we first performed OER and  $CO_2R$  separately in an H-type electrolyzer with control temperatures from  $10^\circ\text{C}$  to  $80^\circ\text{C}$  (for the anode) and from  $10^\circ\text{C}$  to  $60^\circ\text{C}$  (for the cathode). As shown in Fig. 2a (EIS and ECSA tests in Supplementary Figs. S12 and S13), the OER  $I-V$  curves, measured using a H-type electrolyzer with  $IrO_2-Ti$  as the working electrode and 1M KOH as the electrolyte, move to the left side with increasing temperatures. The onset potential under  $10\text{ mA cm}^{-2}$  reduced from  $1.6\text{ V vs. RHE}$  to  $1.5\text{ V vs. RHE}$  as temperature increased from  $10^\circ\text{C}$  to  $80^\circ\text{C}$ . Meanwhile, the Tafel slope decreased from  $201\text{ mV dec}^{-1}$  to  $113\text{ mV dec}^{-1}$  accordingly, suggesting a monotonic performance enhancement with increasing temperature (as shown in the inset figure of Fig. 2a). Note that the slope also decreased in the ohmic region, typically  $\geq 100\text{ mA cm}^{-2}$ , which can be related to the increased electrolyte conductivity at higher temperatures<sup>26</sup> (Fig. 2c). In contrast to the OER, the higher temperature operation of  $CO_2R$ , in general, leads to reduced performance<sup>27</sup> (Fig. 2b and Supplementary Figs. S14–S16). We employed an Ag foil as the working electrode to investigate the effect of temperature on the limiting current density (mass transfer limitation) of  $CO_2R$  in the typical H-type electrolyzer without  $iR$  compensation. To validate the accuracy and reliability of our data, we performed an 85%  $iR$  compensation for the  $20^\circ\text{C}$  data (red curve in Fig. S17) exhibited well-matched electrochemical behavior with existing literature data<sup>28–31</sup>. The  $FE_{CO}$  reduced with the increasing temperature mainly due to reduced



solubility of CO<sub>2</sub> (Fig. 2c) in electrolyte as well as enhanced HER. As the temperature increases, the corresponding saturated vapor pressure of water also rises, making the active sites on the catalyst surface more likely to favor the HER over CO<sub>2</sub>R. The corresponding limiting current density reduced from 10.7 mA cm<sup>-2</sup> to ~0 mA cm<sup>-2</sup> when increasing the temperature from 10 °C to 60 °C.

Experimental verifications were then conducted in the MEA electrolyzer with 0.5 mg cm<sup>-2</sup> Ag-NPs as the cathode and IrO<sub>2</sub>-Ti as the anode under various isothermal and non-isothermal conditions (Fig. 2d and Supplementary Fig. S18). To get the overall electrochemical performance of the MEA electrolyzer, two-electrode measurements for the cell voltages were reported. As shown in Fig. 2d, in

**Fig. 1 | Schematics of the MEA-based CO<sub>2</sub>RR electrolyzer and the performance prediction of non-isothermal operation.** **a** Schematic of the MEA electrolyzer for CO<sub>2</sub> reduction into CO includes two Ti plates with water channels for temperature control and a serpentine flow channel for reactant feed and product discharge. The anodic and cathodic Ti plates sandwich the IrO<sub>2</sub>-Ti anode, anion exchange membrane, Ag-NPs cathode, and PTFE gaskets to form the electrolyzer. **b** Schematic of the reaction and ion transport mechanism for the non-isothermal case for CO<sub>2</sub>RR.

K<sup>+</sup> migrates from the anode to the cathode side, while it can be back transferred by diffusion and thermal diffusion. **c** The predicted electrochemical performance of the MEA electrolyzer under various alkalinities utilizing a multi-physical model. The salt saturation is defined as the ratio of the highest local salt concentrations to the saturation concentration of K<sub>2</sub>CO<sub>3</sub>, and the green circles represent the salting-out current density. **d** The energy efficiency as a function of various cathodic and anodic temperatures. Source data is provided as a Source Data file.

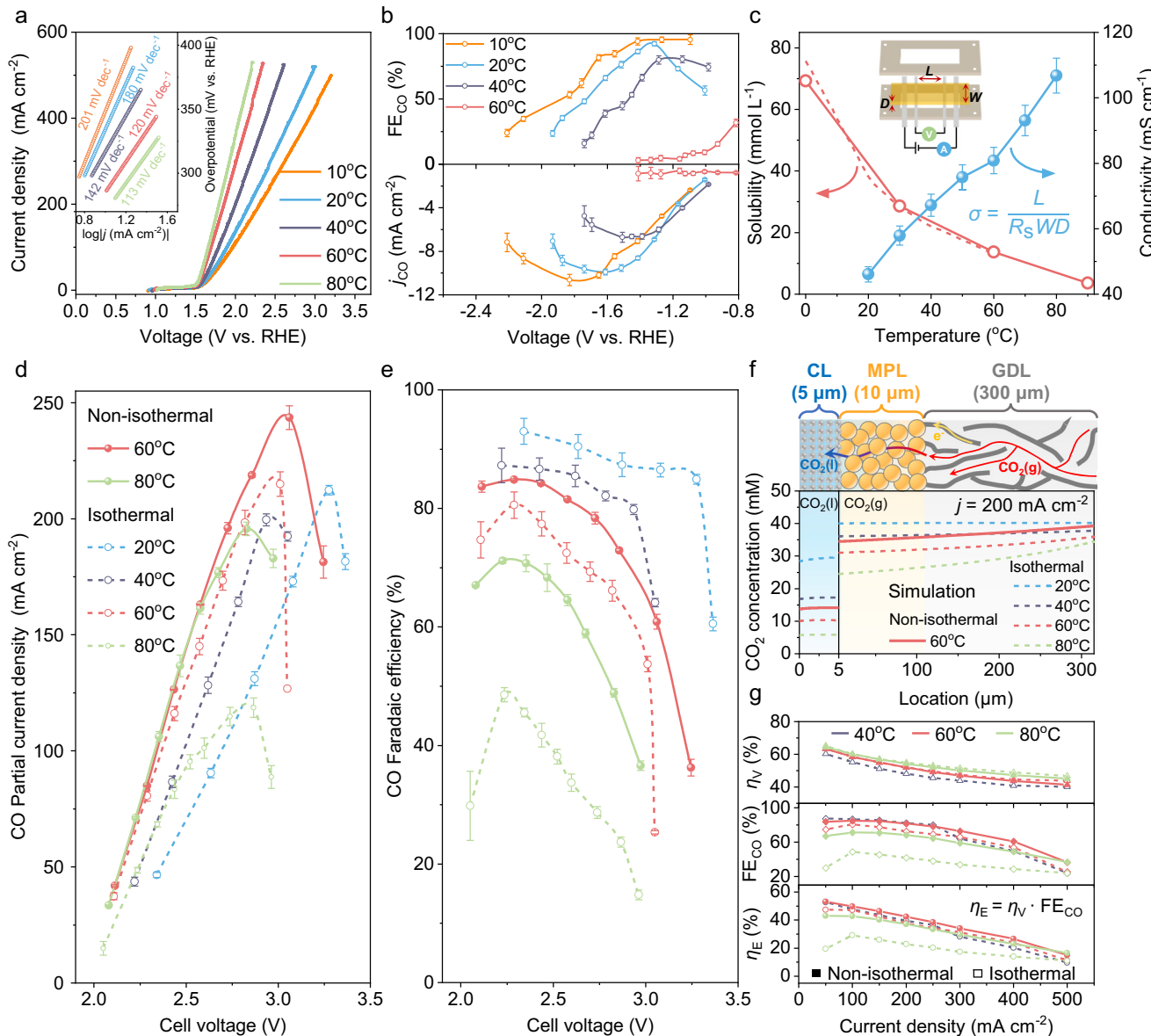


**Fig. 2 | Electrochemical performance evaluation under various cathode and anode temperature combinations and concept verification using a MEA-based electrolyzer.** **a** Linear sweep voltammetry measurement for OER with Tafel slopes shown in the inset figure for a three-electrode H-type cell consisted of IrO<sub>2</sub>-Ti as the working electrode, platinum film as the counter electrode, and Hg/HgO as the reference electrode. **b** CO<sub>2</sub>R intrinsic performance, FE<sub>CO</sub>, and  $j_{CO}$ , on Ag film electrode as a function of temperature in H-type electrolyzer without  $iR$  compensation. The catalytic reaction leans toward hydrogen evolution at high temperature, thereby undermining product selectivity and CO partial current density. **c** Influence of temperature on ionic conductivity of anion exchange membrane (blue line) measured by four-electrode method as well as CO<sub>2</sub> solubility in water

(red dash line<sup>55</sup> and solid line<sup>56</sup>). Characteristics of electrochemical performance with CO partial current density (**d**) and CO Faradaic efficiency (**e**) in isothermal and non-isothermal operations with an Ag-NPs cathode and IrO<sub>2</sub>-Ti anode using 1 M KOH as the anolyte for CO<sub>2</sub> conversion into CO. **f** Schematic of the GDE configuration of the multi-physics model composed of a 5  $\mu$ m catalyst layer (CL), a 10  $\mu$ m micro porous layer (MPL), and a 300  $\mu$ m gas diffusion layer (GDL). The liquid CO<sub>2</sub> concentration is mainly in the CL and MPL with the magnitude inversely related to temperature. **g** Voltage efficiency ( $\eta_V$ ), CO Faradaic efficiency (FE<sub>CO</sub>), and energy efficiency ( $\eta_E$ ) as a function of current density under various isothermal and non-isothermal cases. Source data are provided as a Source Data file.

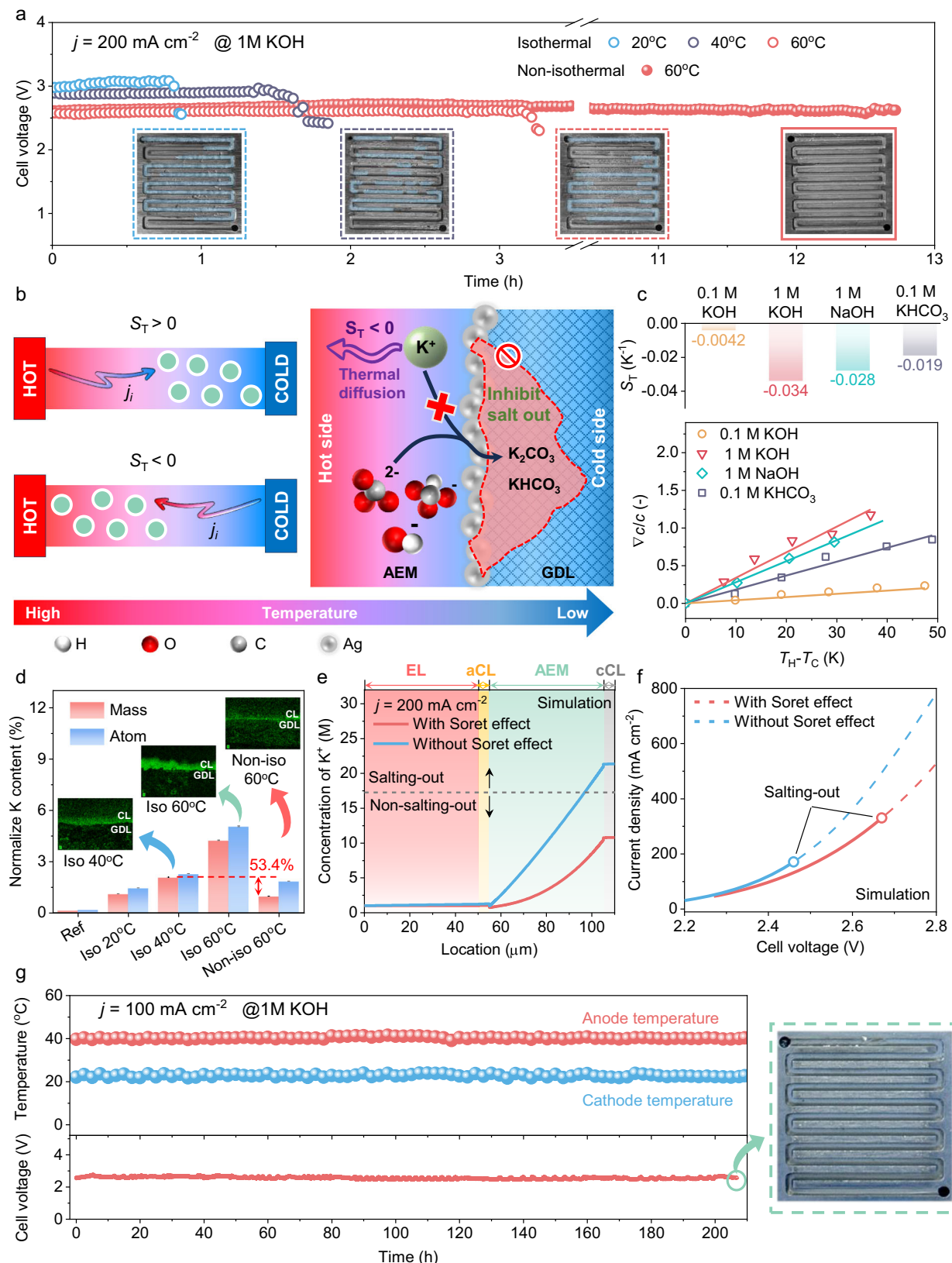
general, the CO partial current density ( $j_{CO}$ ) reaches a maximum value and then decreases with a further increase in cell voltage due to gradually depletion of  $CO_2$  and dominating of HER. For isothermal cases, increasing the electrolyzer operation temperature in the range from 20 °C to 60 °C led to the left shift of curves and a relatively unchanged maximum  $j_{CO}$  (212.3–214.9 mA cm<sup>-2</sup>) suggesting a better electrolyzer performance. While further increasing the temperature to 80 °C, the maximum  $j_{CO}$  dropped sharply to 118.6 mA cm<sup>-2</sup> with a relative reduction of 44.8% compared to the isothermal 60 °C case. This maximum  $j_{CO}$  reduction can be attributed to the low  $CO_2$  solubility at 80 °C (Fig. 1c) and boosted HER (hence reduced  $FE_{CO}$ , Fig. 2e) leading to reduced limiting current density of  $CO_2$ R. Significant performance enhancement was observed for non-isothermal cases (Fig. 2d). The non-isothermal 60 °C case showed 13% increase in maximum  $j_{CO}$ , 243.6 mA cm<sup>-2</sup>, compared to isothermal 60 °C case. Moreover, the non-isothermal 80 °C showed 65% increase in maximum  $j_{CO}$ , from 118.6 mA cm<sup>-2</sup> to 195.6 mA cm<sup>-2</sup>, compared to the isothermal 80 °C case. This verified the effectiveness of our non-isothermal operation strategy that the hotter anode benefits from high activity and a colder cathode leads to higher  $FE_{CO}$ . As seen in Fig. 2e, the  $FE_{CO}$  curves for non-isothermal cases are closer to the isothermal cases with identical cathode temperatures. Similar behavior can be observed in low-concentration and neutral electrolyte systems, such as 0.1M  $KHCO_3$  (see detailed in Supplementary Fig. S19). We have compared our results with recently published literature using Ag catalyst to demonstrate that our experimental outcomes are within a reasonable range in both KOH and  $KHCO_3$  anolyte<sup>21,32–38</sup> (Supplementary Fig. S20). Note that due to imperfect temperature control, the slight discrepancy between the isothermal and non-isothermal cases with the same cathode temperature are not perfectly overlapping (see Supplementary Fig. S21 for detailed temperature profiles). Ideally, further enhancement in the temperature difference can improve the electrolyzer performance as discussed in Fig. 1d. However, in practical scenarios, further increase in temperature difference between anode and cathode is hindered by heat leakage through the thin membrane (Sustainion X37-50 RT, 50 μm) resulting in a maximum temperature difference of -20 °C (Supplementary Fig. S21). Further improvements, including a lower thermal conductivity membrane and a thicker membrane with high ionic conductivity, are needed to push the performance limits (discussed in Fig. 4a–f). We further quantified the  $CO_2$  concentrations in the gas diffusion electrodes under various isothermal and non-isothermal conditions (Fig. 2f). At 200 mA cm<sup>-2</sup>, the  $CO_2(g)$  reduced gradually in GDL and MPL when the location was closer to the CL. The  $CO_2(g)$  in both GDL and MPL is, in general, lower with increased temperature due to the higher saturated vapor pressure of water. At CL, the non-isothermal 60 °C case shows higher  $CO_2(l)$  than the isothermal 60 °C case, while smaller than the isothermal 40 °C case, verifying that the non-isothermal cases can be beneficial for  $CO_2$  mass transport. The optimized energy efficiency ( $\eta_E = \eta_V \cdot FE_{CO}$ ), which combines voltage efficiency ( $\eta_V = E_0/V_{cell}$ ) and CO Faradaic efficiency ( $FE_{CO}$ ), was observed in the non-isothermal 60 °C case. This was attributed to the higher  $FE_{CO}$  compared to the isothermal 60 °C and 80 °C cases, and to the improved voltage efficiency compared to the isothermal 40 °C case (see Fig. 2g). These results suggest beneficial synergies that enhance both mass and charge transfer. Additionally, the COER overpotential is influenced by the cathode temperature, with higher temperatures accelerating reaction kinetics and consequently reducing the overpotential (see Supplementary Fig. S22). The  $\eta_E$  can be improved with an average increment of 4% in the non-isothermal 60 °C case compared to the isothermal 60 °C case, while that of 14% in the non-isothermal 80 °C case compared to the isothermal 80 °C case.

#### Anti-precipitation performance and long-term stability

Our proposed non-isothermal  $CO_2$  reduction ( $CO_2$ R) strategy uniquely offers exceptional anti-precipitation performance under high current

densities and highly alkaline conditions. Here, we compared the anti-precipitation performance for both isothermal and non-isothermal cases using highly alkaline anolyte, i.e., 1M KOH, dry  $CO_2$  gas with a low flow rate of 20 sccm, at 200 mA cm<sup>-2</sup> (Fig. 3a and Supplementary Figs. S23–S25). The isothermal 20 °C case showed electrolyzer failure after 0.8 h due to salting out in the cathode channels. For isothermal cases, the rise in the operation temperature led to a better anti-precipitation performance with a longer lifetime. At 60 °C, the lifetime increased by 300% and reached 3.2 h compared to the isothermal 20 °C case. Similar results were observed with neutral electrolyte (0.1M  $KHCO_3$ ), where salt precipitation occurred after 10 h in the isothermal 40 °C case but was absent in the non-isothermal 40 °C system (Supplementary Fig. S19). The salting-out phenomenon can be directly linked to the migration of  $K^+$  from the anode to the cathode. Our multi-physical model predicted consistent trends in salt precipitation behavior across different isothermal conditions (Supplementary Discussion S2).

Notably, our non-isothermal strategy, e.g., the non-isothermal 60 °C case, shows no salting-out even after 13 h's operation. The enhanced performance is attributed to the backward diffusion of  $K^+$  induced by the temperature gradient, known as the Soret effect, which counteracts the migration of  $K^+$  to the cathode, thereby alleviating salt precipitation (Fig. 3b). The Soret effect describes the migration of substances within a solution in response to a temperature gradient, leading to a non-uniform concentration distribution. This behavior depends on factors such as solution concentration, temperature, particle size, and the physical and chemical properties of the system<sup>22</sup>. The Soret effect is governed by the Soret coefficient ( $S_T$ ) defined as the ratio of the Fickian diffusion coefficient and the thermal diffusion coefficient,  $S_T = D_T/D$ . Particles with  $S_T > 0$  migrate from hot to cold regions, indicating thermophobic behavior, while particles with  $S_T < 0$  exhibit thermophilic behavior by migrating toward warmer regions. Soret effect is reported to be much stronger in the polymer electrolyte than otherwise aqueous electrolyte, typically a Soret coefficient is 1 order of magnitude higher than that in the aqueous solutions<sup>39–41</sup>. Here we measured the Soret coefficient of 1M KOH in the anion exchange membrane (Sustainion imidazolium-functionalized polymers)<sup>42</sup> using a steady-state voltage measurement method (Supplementary Discussion S1 and Figs. S26 and S27). As shown in Fig. 3c, the linear regression linking the ratio of solute molarity difference ( $\nabla c$ ) and initial molarity ( $c$ ) with the temperature difference leads to  $S_T$  of -0.034 K<sup>-1</sup> (opposite number of slope) in the 1M KOH case. This study examined the influence of electrolyte concentration and type on the  $S_T$ . The experimental findings indicate the following: (i) the  $S_T$  becomes increasingly negative with increasing electrolyte concentration, ranging from -0.0042 K<sup>-1</sup> for 0.1M KOH to -0.034 K<sup>-1</sup> for 1M KOH. (ii)  $S_T$  varies with electrolyte, i.e., the  $S_T$  for 1M KOH (-0.034 K<sup>-1</sup>) is more negative than that for 1M NaOH (-0.028 K<sup>-1</sup>), while the  $S_T$  for 0.1M  $KHCO_3$  (-0.019 K<sup>-1</sup>) is also more negative compared to 0.1M KOH (-0.0042 K<sup>-1</sup>). In KOH solution, a negative Soret coefficient indicates that both  $K^+$  and  $OH^-$  ions migrate towards the high-temperature region to maintain electrical neutrality.  $K^+$  concentration is especially important as it can be directly linked to the salt concentration, i.e.,  $K_2CO_3$ , at the cathode, which dictates the salting precipitation behavior. At elevated temperatures, the stability of the  $K^+$  solvation shell is compromised due to the increased molecular motion of water, leading to partial dissociation of the solvation shell. This reduction in stability facilitates the migration of  $K^+$  ions toward the higher temperature region, where their movement is less restricted. Additionally, the decreased solvent density in the high-temperature region further diminishes the retention of  $K$  in the lower-temperature region, promoting their migration toward the hotter area. Regarding ion-ion interactions, the interaction between  $K^+$  and  $OH^-$  may weaken at elevated temperatures, making  $K^+$  ions more prone to migrate toward the high-temperature region<sup>22,43</sup>. The reduced  $K^+$  content at GDE can also



be confirmed by experimentally measuring  $\text{K}^+$  content using energy-dispersive X-ray spectroscopy (EDS) mapping (Fig. 3d and Supplementary Fig. S28). The reference sample (Ref, a pristine sample without operation) is also shown for comparison. The  $\text{K}^+$  content can be directly linked to the accumulated  $\text{K}^+$  at the cell failure. As seen in Fig. 3a, for all isothermal cases, the  $\text{K}^+$  content increased with

temperature. This can be explained by the fact that the solubility of  $\text{K}_2\text{CO}_3$  is enhanced with temperature. For example, the solubility of  $\text{K}_2\text{CO}_3$  is 8.3 M at 20 °C and increases to 10.5 M at 60 °C. For comparison, we showed the best-performing case, which was noted as the non-isothermal 60 °C case in this study, that the  $\text{K}^+$  is 53.4% less than the 40 °C. Note that in non-isothermal 60 °C, the cathode temperature

**Fig. 3 | Impact of Soret effect on anti-precipitation performance.** **a** Anti-precipitation performance test of isothermal 20 °C, 40 °C, 60 °C, and non-isothermal 60 °C cases. The insets are the diagrams of salt precipitation in the cathode channel, with salt marked with blue domains and the corresponding temperature conditions with dashed boxes. **b** Schematic of the Soret effect induced thermal diffusion in non-isothermal cases. The direction of thermal diffusion is determined by the sign of the Soret coefficient ( $S_T$ ). The mass flux of  $K^+$  will be from the cold side to the hot side when the sign of  $S_T$  is negative, which can effectively reduce the  $K^+$  concentration and consequently alleviate the salt precipitation. **c**  $\nabla c/c$  as a function of various temperature differences, with the negative value of the slope representing  $S_T$ . **d** Characterization of mass (red bar) and atom (blue bar) content of K by EDS. The

inset diagrams are the K distributions on the cross-section of GDE. **e** The simulated  $K^+$  distribution within the MEA electrolyzer with (red line) or without (blue line) Soret effect. In the non-isothermal 60 °C case with a constant current density of 200  $mA\ cm^{-2}$ , a  $K^+$  concentration of 17.3 M serves as a threshold to distinguish the occurrence of salt precipitation. **f** The relationship between current density and cell voltage (solid line for salting-out free cases and dashed lines for salting-out cases). **g** Stability test of the MEA electrolyzer in 1 M KOH at a constant current density of 100  $mA\ cm^{-2}$  over 200 h for the non-isothermal 40 °C case (solid red circles are for the anode temperature and solid blue circles are for the cathode temperature). The product composition measurements and anolyte refreshment were performed every 40 h. The photograph of the cathode channel shown on the right side was captured after a 200 h stability test. Source data is provided as a Source Data file.

is ~40 °C. Hence, it is a fair comparison to also compare to the isothermal 40 °C case, which supports our argument that the  $K^+$  is reduced in this non-isothermal strategy. The similar K content at the isothermal 20 °C case and the non-isothermal 60 °C case does not result in salt precipitation at the non-isothermal 60 °C case due to higher salt solubility at elevated temperatures.

Our modeling results also show that the Soret effect can drastically reduce the  $K^+$  concentration from 21.4 M (without Soret effect) to 10.8 M which is lower than the precipitation concentration of 17.28 M (corresponding to the solubility of  $K_2CO_3$ )<sup>44</sup> on the catalyst layer under 200  $mA\ cm^{-2}$  (Fig. 3e), and consequently suppressed the salt precipitation (see Supplementary Fig. S29 for the concentration distributions of  $K^+$  and  $OH^-$ ). This also pushed the salting out point to higher current density, 171  $mA\ cm^{-2}$  without Soret effect vs. 330  $mA\ cm^{-2}$  with Soret effect as seen in Fig. 3f.

The non-isothermal operation strategy of the MEA-based electrolyzer was further assessed for its long-term reliability in preventing salt precipitation. As shown in Fig. 3g and Supplementary Fig. S30, the long-term stability test for the non-isothermal 40 °C case performed at 100  $mA\ cm^{-2}$  with 1 M KOH operated stably over 200 h. The average cell voltage was 2.6 V during the stability test without notable voltage fluctuations (standard deviation of 0.065 mV). The measured cathode and anode temperatures are also shown in Fig. 3g, indicating a stable thermal management. As expected, we observed no salting-out phenomena in the cathode channels (Fig. 3g, right side) after 200 h test. Note that higher current densities beyond 100  $mA\ cm^{-2}$  can be achieved but with limited stable operation time, typically <10 h in literature<sup>35–37,45–48</sup> (Supplementary Table S6 and Fig. S31). We observed an absolute  $FE_{CO}$  reduction of 18% from 86% to 68% after 80 h, attributed to the enhanced hydrophilicity of the carbon paper (see Supplementary Fig. S25). This performance outperforms most existing literature reports, typically a  $FE_{CO}$  reduction of ~20% after 50 h<sup>35,49,50</sup>.

### Further performance improvement

In practice, the performance of the MEA-based electrolyzer can be further improved by increasing the anode and cathode temperature difference. This can be achieved by either increasing the membrane thickness or decreasing the membrane thermal conductivity. Figure 4a shows the temperature differences, CO Faradaic efficiency, and energy conversion efficiency as a function of membrane thickness at 200  $mA\ cm^{-2}$ . Large membrane thickness enables higher temperature differences between the anode and the cathode, which results in higher  $FE_{CO}$  due to lower cathode temperature. However, the increased membrane thickness led to increased membrane ohmic overpotential, which dominates the energy loss and hence leads to decreased energy efficiency. To benefit from the enlarged temperature difference by increasing the membrane thickness, we expect to have a better-performing membrane with higher ionic conductivity. By artificially increasing the ionic conductivity of the membrane, the energy efficiency increases with the increasing conductivity for a specific thickness (as seen in Fig. 4b and Supplementary Figs. S32 and S33). With increasing membrane thickness, the energy efficiency firstly

increases, due to increased Faradaic efficiency (FE controlled region), to a peak value (dashed line), and then decreases, due to increased ohmic overpotential (ohmic controlled region) with further increase in thickness. The ohmic controlled region narrowed at higher ionic conductivity. Correspondingly, due to the increase in ohmic impedance by increasing the membrane thickness (Supplementary Figs. S34 and S35), the salting-out current density is, in general, lower at larger thicknesses (Fig. 4c). The salting-out current density can be increased by increasing the membrane ionic conductivity. For example, for a typical membrane thickness of 50  $\mu m$ , the expected ionic enhancement should be larger than 3 in order to achieve a salting-out current density larger than 1  $A\ cm^{-2}$ .

Alternatively, an enlarged temperature difference can be achieved by reducing the thermal conductivity of the membrane (Fig. 4d and Supplementary Fig. S36). As a result, the  $FE_{CO}$  can be enhanced at lower thermal conductivity. Note that even lower (<10<sup>-3</sup>  $W\ m^{-1}\ K^{-1}$ ) thermal conductivity is not necessary. Figure 4e shows that lowering both membrane thickness and thermal conductivity leads to higher energy efficiency. Note that it is less unlikely we can find a membrane with thermal conductivity at 10<sup>-3</sup>  $W\ m^{-1}\ K^{-1}$  level, a reasonable energy efficiency can be achieved by only reducing the thermal conductivity by 10 times. For example, at 50  $\mu m$ , the energy efficiency increased from 40% to 43% when the thermal conductivity decreased from 0.2  $W\ m^{-1}\ K^{-1}$  (the present experimental value) to 0.02  $W\ m^{-1}\ K^{-1}$ . This thermal conductivity can be potentially achieved by introducing an advanced aerogel-based membrane<sup>51</sup>. The salting-out current density also increases with decreasing thermal conductivity and membrane thickness. For a thinner membrane thickness of 25  $\mu m$ , the thermal conductivity should be smaller than 0.02  $W\ m^{-1}\ K^{-1}$  to achieve a salting-out current density larger than 1  $A\ cm^{-2}$  (see Fig. 4f). To estimate the energy consumption to maintain the temperature of both sides in the optimized case, we did a detailed energy balance analysis (see the Supplementary Discussion S3) and concluded that the additional energy required for the thermal management only accounts for ~5% of the total energy input into the device. To scale up, we proposed two stack designs to realize our non-isothermal thermal management, including a water cooling/heating strategy with a parallel connection and a direct cooling/heating strategy with a series connection (see Supplementary Fig. S37). A 100  $cm^2$  device is also experimentally demonstrating that a stable temperature difference of 20 °C can be maintained, indicating the scalability potential of our strategy (see Supplementary Fig. S41).

The non-isothermal strategy effectively enhances electrical efficiency and mitigates salt precipitation, though it also introduces additional thermal energy losses. To assess the economic feasibility and adaptability of this approach, we conducted a techno-economic analysis (TEA) (model details in Supplementary Discussion S4)<sup>25</sup>. As shown in Fig. 4g, the CO production cost in the non-isothermal 60 °C case is 0.41  $\$/kg^{-1}$ , compared to 0.47  $\$/kg^{-1}$  at ambient temperature, i.e., the isothermal 20 °C case. The non-isothermal strategy requires additional thermal energy costs (45.93  $\$/day^{-1}$ ) for startup heating and to maintain the non-isothermal state. However, the MEA

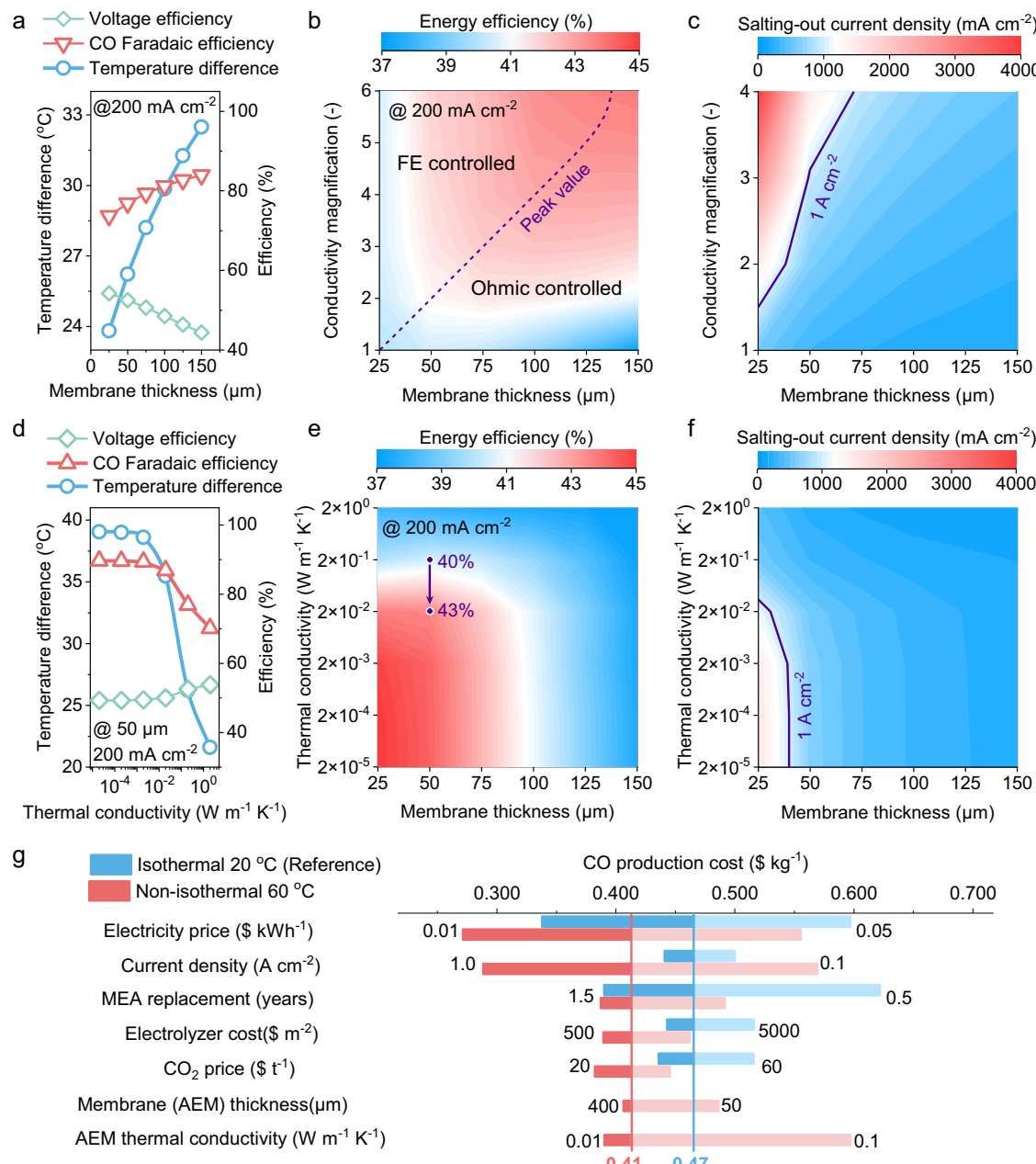


**Fig. 4 | Further improvement strategies.** **a** The model predicted temperature difference (blue curve) and efficiency, including voltage efficiency (green curve) and CO Faradaic efficiency (red curve) as a function of membrane thickness under a typical current density of  $200 \text{ mA cm}^{-2}$ . **b** The effects of membrane thickness and ionic conductivity at  $200 \text{ mA cm}^{-2}$ . The purple dashed line indicates the peak value of energy efficiency at the corresponding thickness. **c** Contour plot of the salting-out current density as a function of ionic conductivity magnification and membrane thickness. The purple contour indicates the conditions required to achieve  $1 \text{ A cm}^{-2}$  current density. **d** The model predicted temperature difference (blue curve) and efficiency, including voltage efficiency (green curve) and CO Faradaic

efficiency (red curve) as a function of thermal conductivity under a typical current density of  $200 \text{ mA cm}^{-2}$ . **e** Energy efficiency as a function of thermal conductivity and membrane thickness. When the thermal conductivity was reduced by an order of magnitude compared to the reference case condition of  $0.2 \text{ W m}^{-1} \text{ K}^{-1}$  thermal conductivity, the energy efficiency was increased from 40% to 43% under  $50 \mu\text{m}$  membrane thickness. **f** Contour plot of the salting-out current density as a function of thermal conductivity and membrane thickness. **g** Techno-economic with single-variable sensitivity analysis for the CO production cost under the comparison of the reference case (blue bars) and non-isothermal  $60^\circ\text{C}$  case (red bars). Source data are provided as a Source Data file.

replacement costs associated with desalination operation are  $154.92 \text{ } \$ \text{ day}^{-1}$  in the reference case compared to  $77.46 \text{ } \$ \text{ day}^{-1}$  in the non-isothermal  $60^\circ\text{C}$  case. The CO production cost is able to further reduce as electricity prices decrease, current density increases, or membrane performance is optimized (Supplementary Fig. S38). For instance, at a current density of  $1 \text{ A cm}^{-2}$ , the cost of the non-isothermal strategy can be reduced to  $0.28 \text{ } \$ \text{ kg}^{-1}$ . A decrease in electricity price can offset the thermal energy cost in the non-

isothermal case. The CO production cost will fall to  $0.27 \text{ } \$ \text{ kg}^{-1}$  when the electricity price is up to  $0.01 \text{ } \$ \text{ kWh}^{-1}$ . Based on the TEA model, we analyzed the impact of the membrane performance of thermal conductivity and thickness on CO production costs (Supplementary Fig. S39). A membrane with lower thermal conductivity and greater thickness can reduce CO production costs. For instance, at  $1 \text{ A cm}^{-2}$  and a thermal conductivity of  $0.02 \text{ W m}^{-1} \text{ K}^{-1}$ , the cost is  $0.20 \text{ } \$ \text{ kg}^{-1}$  lower compared to isothermal conditions at  $20^\circ\text{C}$ . Similarly, at  $1 \text{ A cm}^{-2}$  and a thermal conductivity of  $0.02 \text{ W m}^{-1} \text{ K}^{-1}$ , the cost is  $0.20 \text{ } \$ \text{ kg}^{-1}$  lower compared to isothermal conditions at  $20^\circ\text{C}$ . Similarly, at  $1 \text{ A cm}^{-2}$  and a thermal conductivity of  $0.02 \text{ W m}^{-1} \text{ K}^{-1}$ , the cost is  $0.20 \text{ } \$ \text{ kg}^{-1}$  lower compared to isothermal conditions at  $20^\circ\text{C}$ .

and a membrane thickness of 300  $\mu\text{m}$ , the cost is also 0.20 \$  $\text{kg}^{-1}$  lower compared to isothermal conditions at 20 °C. To further demonstrate the potential of the non-isothermal strategy, we compared it with existing desalination methods (detailed in Supplementary Discussion S5 and Fig. S40, such as using low-concentration electrolytes (0.1 M  $\text{KHCO}_3$  and 0.01 M  $\text{KHCO}_3$  with CO cost of 0.42 and 0.62 \$  $\text{kg}^{-1}$ ), pulse voltage methods (0.51 \$  $\text{kg}^{-1}$ ), and increasing gas flow rates (0.69 \$  $\text{kg}^{-1}$ ). Our findings present that the non-isothermal strategy demonstrates greater economic potential and opportunities for CO production cost.

## Discussion

In this work, we propose an innovative approach involving thermal management for separate temperature control for the anode and cathode, forming a non-isothermal MEA by maintaining an elevated anodic temperature while cooling the cathode. This approach simultaneously addresses the need for a high-temperature anode with higher reaction kinetics and a low-temperature cathode to maintain a high  $\text{CO}_2$  solubility and to suppress HER. Owing to the negative Soret coefficient of KOH electrolyte with AEM for electrochemical  $\text{CO}_2$  reduction, the  $\text{K}^+$  flux tends to move from cold cathode to hot anode via thermal diffusion in the non-isothermal case to suppress the combination of  $\text{K}^+$  and  $\text{CO}_3^{2-}/\text{HCO}_3^-$ , which can essentially solve the salt precipitation problem. The optimal performance was found to be the non-isothermal 60 °C case, yielding a  $j_{\text{CO}}$  of 243.6 mA  $\text{cm}^{-2}$  at 3.2 V, marking a 13% improvement over the isothermal 60 °C scenario ( $j_{\text{CO}} = 214.9 \text{ mA cm}^{-2}$ ). Due to the anti-precipitation capacity of salt accumulation, the durability of zero-gap MEA can achieve over 200 h for the non-isothermal 40 °C case in 1 M KOH. This study presents an efficient non-isothermal operation for advanced thermal management for MEA-based  $\text{CO}_2$  electrolyzers for simultaneous enhancement in anode activity as well as cathode selectivity. Future improvement requires an enlarged Soret effect by further tuning membrane properties such as reduced thermal conductivity and enhanced ionic conductivity. Furthermore, our techno-economic analysis indicates that this strategy significantly reduces  $\text{CO}_2$  production costs, demonstrating its economic feasibility for large-scale deployment.

## Methods

### Chemicals and materials

Potassium hydroxide (KOH, 99.99%, metals basis), potassium chloride (KCl, 99.8%), and silver-nanoparticle powders (Ag-NP, 99.5%, metals basis, 60–120 nm) were purchased from Aladdin. Potassium bicarbonate ( $\text{KHCO}_3$ , 99.7%) was purchased from Sigma-Aldrich and used as received. Absolute ethyl alcohol ( $\text{CH}_3\text{CH}_2\text{OH}$ , 99.5%, with molecular sieves, water <50 ppm) was purchased from Acme-Biochemical. Alkaline Ionomer (Sustainion® XA-9, 5% in ethanol mixture) was purchased from Dioxide Materials for cathode preparation. Silver film (Ag, 99.99%), platinum film (Pt, 99.99%), glass Ag/AgCl reference electrode, and Hg/HgO reference electrode were purchased from Tjaida. Chloro-iridic acid ( $\text{IrCl}_6$ ) and titanium fiber felts (Ti, 0.25 mm thickness, 0.25 porosity) were purchased from Yiwantin-Tech for anode preparation. The carbon paper (Sigracet 28BC, 5 wt% PTFE) consisted of a microporous layer (MPL) covering a gas-diffusion layer (GDL) was purchased from SGL Carbon. Anion exchange membrane (AEM, Sustainion® X37-50 grade RT membrane, Dioxide Materials) was purchased from Dioxide Materials and stored in 1 M KOH before use. Argon (Ar, 99.999%, as GC carrier gas), nitrogen ( $\text{N}_2$ , 99.999%), and carbon dioxide ( $\text{CO}_2$ , 99.999%) were purchased from Huateng. All chemicals and materials were used as received. The Milli-Q water with a resistivity of 18.2 M $\Omega$   $\text{cm}^{-1}$  was used for all aqueous solution preparation. All electrolytes were prepared fresh prior to use and stored in a cool, dark environment when necessary.

### Electrode preparation

To prepare a gas diffusion electrode (GDE) as a cathode, the Ag-NPs were sprayed on the catalyst layer (MPL of carbon papers). All the GDE electrodes used in this study were  $1.5 \times 1.5 \text{ cm}^2$ . In total, 3.2 mg of Ag-NP powders were diluted with 2.5 mL of ethyl alcohol and high-power sonicated prior to use. In total, 25  $\mu\text{L}$  ionomer solution (XA-9) was added to the solution and further sonicated for 1 h until homogeneous dispersion was achieved. The solution was then sprayed-coated evenly via the spray gun onto the carbon paper substrate on the 80 °C hot platform to achieve a desired Ag-NPs loading of ~0.5 mg  $\text{cm}^{-2}$ .

The anodes were made of depositing  $\text{IrO}_2$  onto a titanium fiber felt via the method of dip coating and thermal decomposition. Typically, the titanium fiber felt was first purged by absolute ethyl alcohol and deionized water, and then etched in oxalic acid in the condition of 90 °C for 3 h until the surface oxide layer is etched to the surface of titanium hydride. Subsequently, the etched titanium fiber felt was dipped into the  $\text{IrCl}_6$  solution, dried in an oven at 100 °C for 10 min before calcination in a furnace at 500 °C for 1 h, and then cooled naturally to room temperature (~20 °C). The dipping, calcination, and cooling process was repeated to achieve a desired loading of ~2 mg  $\text{cm}^{-2}$ .

### Electrochemical configurations and measurements

The H-type electrolyzer was fabricated from quartz glass, with each chamber having a volume of 30 mL. The room temperature is ~20 °C for all testing. All non-ambient temperature (>20 °C) electrochemical experiments in the H-type electrolyzer used a water bath heating system was employed with continuous temperature monitoring. All the AEMs (50  $\mu\text{m}$ ,  $2 \times 2 \text{ cm}^2$ ) used in this study were soaked in 1 M KOH for 24 h at room temperature, followed by immersion in fresh KOH solution for an additional 24 h to activate, and finally rinsed with deionized water for 5 min before use.

For the oxygen evolution reaction (OER) performance measurement at different temperatures, a H-type electrolyzer without separation was based on a three-electrode configuration, composed of an  $\text{IrO}_2$ -Ti working electrode, a Pt film counter electrode, and a Hg/HgO reference electrode immersed in the 1 M KOH aqueous electrolyte ( $\text{pH} = 14 \pm 0.1$ ). All reference electrode in this study was calibrated using a comparative method against a standard reference electrode in 3.5 M KCl solution through open-circuit potential measurements, with a potential difference <5 mV considered acceptable. The 30 sccm of pure  $\text{N}_2$  was bubbled continuously in the electrolyte to purge gas impurities 1 h prior to and during all electrochemical measurements.

The  $\text{CO}_2$  reduction reaction ( $\text{CO}_2\text{RR}$ ) experiments in the customized gastight H-type electrolyzer separated by anion exchange membrane with 30 mL volume of each chamber were based on three-electrode configuration, composed of an Ag film working electrode, a Pt film counter electrode, and an Ag/AgCl reference electrode immersed in the 0.1 M  $\text{KHCO}_3$  aqueous electrolyte ( $\text{pH} = 8.3 \pm 0.1$ ). The electrolyte is saturated with a pH of  $6.8 \pm 0.1$  by bubbling with high-purity  $\text{CO}_2$  for at least 30 min and keeping the  $\text{CO}_2$  supply at 20 sccm during the experiment. Prior to the experiment, the Ag film electrode was sanded to a smooth surface with 1000 grit sandpaper.

The  $\text{CO}_2$  reduction reaction ( $\text{CO}_2\text{RR}$ ) experiments in the MEA, two-electrode configuration, were performed in a home-made electrolyzer cell. The home-made MEA cell was made from two grade TA-2 titanium polar plates with a serpentine channel for the cathodic and anodic flows ( $1.5 \times 1.5 \text{ cm}^2$  active area), additional internal annular flow channels were designed in each plate for heating or cooling water transportation to tune the electrode temperature. The 50  $\mu\text{m}$  anion exchange membrane was pressed between the Ag-NP cathode and the  $\text{IrO}_2$ -Ti felt-based anode. And two PTFE gaskets of 0.25 mm thickness were assembled to hold the electrodes in position as well as prevent gas and liquid leakage. Six bolt screws were carried out to assemble the cell with a torque of 6 N m in the whole experiments. Except for the

anti-precipitation performance test of the cathode purged continuously with 20 sccm dry CO<sub>2</sub> and anode fed with 5 mL min<sup>-1</sup> 1 M KOH electrolyte, all of the experiments were performed by supplying 50 sccm humidified CO<sub>2</sub> into the cathode serpentine flow-channel controlled by a mass flow controller (Beijing Sevenstar Electronics Co., Ltd., CS200, accuracy  $\leq \pm 1\%$ ) and circulating 1 M KOH electrolyte at 10 mL min<sup>-1</sup> pumped by peristaltic pumps. Each electrode plate was designed with an internal annular flow channel (6.2 mm diameter) around the reaction area chamber for thermal management via circulating deionized water. A water heater (Tianlin, temperature range -20 °C to 100 °C, temperature fluctuation 0.05 °C) and a chiller (Hongsen, temperature range 0–40 °C, temperature fluctuation 3 °C) at a constant flow rate of 250 mL min<sup>-1</sup> through peristaltic pumps were used to achieve temperature differences. All the temperature measurement was recorded by a data acquisition device (Keithley DAQ6510) through K-type thermocouples (Kaipusen, -40 °C to 260 °C) and T-type thermocouples (Kaipusen, -200 °C to 200 °C).

All the electrochemical measurement was operated under an electrochemical workstation (Gamry, Reference 3000 with 30 A booster). All potential values reported in this study were recorded without *iR* correction. The error bars are obtained from 3 measurements. The reference electrode potentials were converted to reversible hydrogen electrode (RHE) in the three-electrode configuration using the equation of

$$E(\text{vs. RHE}) = E(\text{vs. Ag/AgCl}) + E_{\text{Ag/AgCl}}^0 + \ln 10 \frac{RT}{F} \times \text{pH} \quad (1)$$

$$E(\text{vs. RHE}) = E(\text{vs. Hg/HgO}) + E_{\text{Hg/HgO}}^0 + \ln 10 \frac{RT}{F} \times \text{pH} \quad (2)$$

where  $E_{\text{Ag/AgCl}}^0$  and  $E_{\text{Hg/HgO}}^0$  are standard potentials of reference electrode correlated with temperature<sup>52,53</sup> (see Supplementary Table. S7),  $T$  is the temperature (K),  $F$  is the Faraday constant (96485 C mol<sup>-1</sup>), and  $R$  is the ideal gas constant (8.314 J mol<sup>-1</sup> K<sup>-1</sup>).

### CO<sub>2</sub>RR products analysis

The outlet gas of the electrolyzer was passed through a drying bottle for dehydration and a dry-type gas flowmeter (Beijing Kean Laobao, DCAL 500, accuracy  $\leq \pm 1\%$ ) for recording the volume flow rate of the gas mixture in turn. Subsequently, the gas mixture products were analyzed by an online gas chromatograph (GC, FULI INSTRUMENTS, GC9790Plus) equipped with a Molecular Sieve 5 A Capillary Column, Hayesep A, and Porapak N columns with argon as the carrier gas. A thermal conductivity detector (TCD) operated at 120 °C was employed to quantify the H<sub>2</sub> concentration, and a flame ionization detector (FID) operated at 150 °C was used to analyze the CO concentration. The gas chromatograph was calibrated by sampling a gas mixture of three known concentrations of standard gases compared with the peak area of the instrument analyzed (as shown in Supplementary Fig. S42).

The Faradaic efficiency (FE) of gas products was calculated as follows:

$$\text{FE}_i = \frac{n_i \cdot F \cdot p_0 \cdot x_i \cdot v}{j_{\text{total}} \cdot R \cdot T} \cdot 100\% \quad (3)$$

where  $n_i$  is the number of electrons transferred per mole of gaseous product  $i$  involved in the reaction,  $F$  is Faraday constant (96485 C mol<sup>-1</sup>),  $p_0$  is the standard atmospheric pressure (101.325 kPa),  $x_i$  is the volume fraction of product  $i$  quantified by online gas chromatograph in the cathodic gas mixture,  $v$  is the flow rate calculated by dry-type gas volumetric flowmeter,  $j_{\text{total}}$  is the total current recorded by electrochemical workstation,  $R$  is the ideal gas constant (8.314 J mol<sup>-1</sup> K<sup>-1</sup>), and  $T$  is the temperature. All calculations need to be converted to the International System of Units.

Calculation of partial current density ( $j_i$ ) was determined using the following equation:

$$j_i = \frac{j_{\text{total}} \cdot \text{FE}_i}{A} \quad (4)$$

where  $A$  is the geometric active-area of working electrode.

Calculation of energy efficiency ( $\eta_E$ ) was determined as follow,

$$\eta_E = \eta_V \cdot \text{FE}_{\text{CO}} \quad (5)$$

where  $\eta_E = E_0/V_{\text{cell}}$  is determined as voltage efficiency while the  $E_0 = 1.34$  V is the equilibrium for CO<sub>2</sub>RR in this study and  $V_{\text{cell}}$  is the applied cell voltage for a given geometric current density.

### Electrode characterization

Scanning electron microscope (SEM, Carl Zeiss Microscopy Ltd., Sigma 300) with an integrated energy-dispersive X-ray spectroscopy (EDS) at Department of Earth and Space Sciences in Southern University of Science and Technology was employed to observe the morphology and the elements in the cross-section and surface of porous electrode sample and further analyze the element composition of different conditions, respectively. The X-ray diffraction measurements (XRD) pattern equipped with a 9 KW rotating anode X-ray tube was collected using a Rigaku Smartlab. Contact angle experiments were conducted by using a sessile drop method on a video-based contact angle measuring system (Sindin, SDC-200SH).

### Electrochemical double-layer capacitance measurement

Electrochemical double-layer capacitance ( $C_{\text{dl}}$ ) measurements were carried out in the H-cell with a three-electrode configuration, scanning the potential via cyclic voltammetry (CV) in the non-Faradaic region. The non-Faradaic is typically a voltage window ranging from 100 mV around the open-circuit potential (OCP). Scan rates were various from 20 mV s<sup>-1</sup>, 40 mV s<sup>-1</sup>, 60 mV s<sup>-1</sup>, 80 mV s<sup>-1</sup>, and 100 mV s<sup>-1</sup>. The measured currents recorded from the forward and reverse scans of the 5th cycle at a constant voltage were considered as a result of the double-layer charging, which is given by the equation,

$$i_c = \nu C_{\text{dl}} \quad (6)$$

where  $i_c$  is the charging current and  $\nu$  is the scan rate of the CV measurement. Double-layer capacitance is the slope of the plot as a function of charging current and scan rate. Typically, the electrochemically active surface area (ECSA) was further calculated by  $C_{\text{dl}}$ , as expressed by,

$$\text{ECSA} = \frac{C_{\text{dl}}}{C_s} \quad (7)$$

where  $C_s$  is the specific capacitance, which was reported to range between 0.022 and 0.130 mF cm<sup>-2</sup> in KOH solution<sup>54</sup>.

### Membrane conductivity measurement

The ion conductivity of anion exchange membrane assembled into a four-electrode conductivity cell with a size of 20 × 20 mm was measured by an electrochemical workstation (Gamry RF3000) using alternating current (AC) impedance in the frequency range of 1 MHz to 1 Hz with a voltage amplitude of 10 mV. Membrane samples were immersed three times in the 1 M KOH for at least 12 h each time to exchange the desired anion and washed for at least 5 min with deionized water prior to the measurement. Experiments at 100% RH at temperatures ranging from 20 °C to 80 °C were conducted in deionized water purged with 20 sccm N<sub>2</sub> to avoid the hydroxide combined with CO<sub>2</sub>. The ion conductivity of anion exchange membrane is

expressed by,

$$\sigma = \frac{L}{R_s A} \quad (8)$$

where  $L$  is the length of the membrane between counter and working electrode,  $A = WD$  is the cross-section area of membrane samples, and  $W$  is the width and  $D$  is the thickness,  $R_s$  taken an average of 3 measurements is measured resistance obtained by the Nyquist plots from the electrochemical impedance spectra (EIS) test.

### Soret coefficient measurement

Soret effect refers to the migration of particles assisted by temperature gradients, depending on the parameter known as the Soret coefficient ( $S_T$ ). The  $S_T$  can be calculated as  $S_T = D_T / D$  detailed in Supplementary Discussions S1.

### Multiphysics modeling

A one-dimensional model was developed to simulate the desired phenomena of the electrochemical  $\text{CO}_2$  reduction system, such as ion transport, charge transfer, homogeneous reactions and phase-transfer reactions, gas and liquid transport, and heat transfer. The details for the modeling are shown in Supplementary Discussion S2.

### Data availability

The data for plotting all figures in the paper are provided as supplementary data, and all other data are available from the corresponding author upon request. Source data are provided with this paper.

## References

1. Bushuyev, O. S. et al. What should we make with  $\text{CO}_2$  and how can we make it? *Joule* **2**, 825–832 (2018).
2. Birdja, Y. Y. et al. Advances and challenges in understanding the electrocatalytic conversion of carbon dioxide to fuels. *Nat. Energy* **4**, 732–745 (2019).
3. Boutin, E. et al. Photo-electrochemical conversion of  $\text{CO}_2$  under concentrated sunlight enables combination of high reaction rate and efficiency. *Adv. Energy Mater.* **12**, 2200585 (2022).
4. Shin, H., Hansen, K. U. & Jiao, F. Techno-economic assessment of low-temperature carbon dioxide electrolysis. *Nat. Sustain.* **4**, 911–919 (2021).
5. Fan, L., Xia, C., Zhu, P., Lu, Y. & Wang, H. Electrochemical  $\text{CO}_2$  reduction to high-concentration pure formic acid solutions in an all-solid-state reactor. *Nat. Commun.* **11**, 1–9 (2020).
6. Lees, E. W., Mowbray, B. A. W., Parlante, F. G. L. & Berlinguette, C. P. Gas diffusion electrodes and membranes for  $\text{CO}_2$  reduction electrolyzers. *Nat. Rev. Mater.* **7**, 55–64 (2022).
7. Chen, C., Li, Y. & Yang, P. Address the “alkalinity problem” in  $\text{CO}_2$  electrolysis with catalyst design and translation. *Joule* **5**, 737–742 (2021).
8. Verma, S. et al. Insights into the low overpotential electroreduction of  $\text{CO}_2$  to CO on a supported gold catalyst in an alkaline flow electrolyzer. *ACS Energy Lett.* **3**, 193–198 (2018).
9. Cheng, W. H. et al.  $\text{CO}_2$  Reduction to CO with 19% Efficiency in a solar-driven gas diffusion electrode flow cell under outdoor solar illumination. *ACS Energy Lett.* **5**, 470–476 (2020).
10. Disch, J. et al. High-resolution neutron imaging of salt precipitation and water transport in zero-gap  $\text{CO}_2$  electrolysis. *Nat. Commun.* **13**, 6099 (2022).
11. Wheeler, D. G. et al. Quantification of water transport in a  $\text{CO}_2$  electrolyzer. *Energy Environ. Sci.* **13**, 5126–5134 (2020).
12. Moss, A. B. et al. In operando investigations of oscillatory water and carbonate effects in MEA-based  $\text{CO}_2$  electrolysis devices. *Joule* **7**, 350–365 (2023).
13. Fan, M. et al. Cationic-group-functionalized electrocatalysts enable stable acidic  $\text{CO}_2$  electrolysis. *Nat. Catal.* **6**, 763–772 (2023).
14. Fang, W. et al. Durable  $\text{CO}_2$  conversion in the proton-exchange membrane system. *Nature* **626**, 86–91 (2024).
15. Sassenburg, M., Kelly, M., Subramanian, S., Smith, W. A. & Burdyny, T. Zero-gap electrochemical  $\text{CO}_2$  reduction cells: challenges and operational strategies for prevention of salt precipitation. *ACS Energy Lett.* **8**, 321–331 (2023).
16. Kim, H. et al. A unifying mechanism for cation effect modulating  $\text{C}_1$  and  $\text{C}_2$  productions from  $\text{CO}_2$  electroreduction. *Nat. Commun.* **13**, 5482 (2022).
17. Monteiro, M. C. O. et al. Absence of  $\text{CO}_2$  electroreduction on copper, gold and silver electrodes without metal cations in solution. *Nat. Catal.* **4**, 654–662 (2021).
18. Xu, Y., Xia, Z., Gao, W., Xiao, H. & Xu, B. Cation effect on the elementary steps of the electrochemical CO reduction reaction on Cu. *Nat. Catal.* **7**, 1120–1129 (2024).
19. Endrődi, B. et al. Operando cathode activation with alkali metal cations for high current density operation of water-fed zero-gap carbon dioxide electrolyzers. *Nat. Energy* **6**, 439–448 (2021).
20. El-Nagar, G. A., Haun, F., Gupta, S., Stojkovikj, S. & Mayer, M. T. Unintended cation crossover influences  $\text{CO}_2$  reduction selectivity in Cu-based zero-gap electrolyzers. *Nat. Commun.* **14**, 1–11 (2023).
21. Xu, Y. et al. Self-cleaning  $\text{CO}_2$  reduction systems: unsteady electrochemical forcing enables stability. *ACS Energy Lett.* **6**, 809–815 (2021).
22. Di Lecce, S., Albrecht, T. & Bresme, F. The role of ion-water interactions in determining the Soret coefficient of LiCl aqueous solutions. *Phys. Chem. Chem. Phys.* **19**, 9575–9583 (2017).
23. Han, C. et al. Giant thermopower of ionic gelatin near room temperature. *Science* **368**, 1091–1098 (2020).
24. Giron Rodriguez, C. A. et al. Insights into zero-gap  $\text{CO}_2$  electrolysis at elevated temperatures. *EES Catal.* **2**, 850–861 (2024).
25. Petrov, K. V. et al. Anion-exchange membranes with internal microchannels for water control in  $\text{CO}_2$  electrolysis. *Sustain. Energy Fuels* **6**, 5077–5088 (2022).
26. Wu, X., Chen, N., Klok, H., Lee, Y. M. & Hu, X. Branched poly (aryl piperidinium) membranes for anion-exchange membrane fuel cells. *Angew. Chem. Int. Ed.* **61**, 1–8 (2022).
27. Li, K. et al. Superhydrophobicity-enabled efficient electrocatalytic  $\text{CO}_2$  reduction at a high temperature. *ACS Catal.* **13**, 9346–9351 (2023).
28. Hatsukade, T., Kuhl, K. P., Cave, E. R., Abram, D. N. & Jaramillo, T. F. Insights into the electrocatalytic reduction of  $\text{CO}_2$  on metallic silver surfaces. *Phys. Chem. Chem. Phys.* **16**, 13814–13819 (2014).
29. Zhang, Y. et al. Enhancing  $\text{CO}_2$  electroreduction on nanoporous silver electrode in the presence of halides. *Electrochim. Acta* **313**, 561–569 (2019).
30. Wu, X. et al. Fast operando spectroscopy tracking in situ generation of rich defects in silver nanocrystals for highly selective electrochemical  $\text{CO}_2$  reduction. *Nat. Commun.* **12**, 660 (2021).
31. Kim, C. et al. Achieving selective and efficient electrocatalytic activity for  $\text{CO}_2$  reduction using immobilized silver nanoparticles. *J. Am. Chem. Soc.* **137**, 13844–13850 (2015).
32. Ko, Y. et al. Extrinsic hydrophobicity-controlled silver nanoparticles as efficient and stable catalysts for  $\text{CO}_2$  electrolysis. *Nat. Commun.* **15**, 3356 (2024).
33. Park, J. W. et al. Bimetallic gold–silver nanostructures drive low overpotentials for electrochemical carbon dioxide reduction. *ACS Appl. Mater. Interfaces* **14**, 6604–6614 (2022).
34. Kim, D. et al. Electrocatalytic reduction of low concentrations of  $\text{CO}_2$  gas in a membrane electrode assembly electrolyzer. *ACS Energy Lett.* **6**, 3488–3495 (2021).

35. Lee, W. H. et al. Highly selective and scalable CO<sub>2</sub> to CO - electrolysis using coral-nanostructured Ag catalysts in zero-gap configuration. *Nano Energy* **76**, 105030 (2020).
36. Wang, R. et al. Maximizing Ag utilization in high-rate CO<sub>2</sub> electrochemical reduction with a coordination polymer-mediated gas diffusion electrode. *ACS Energy Lett.* **4**, 2024–2031 (2019).
37. Endrödi, B. et al. Multilayer electrolyzer stack converts carbon dioxide to gas products at high pressure with high efficiency. *ACS Energy Lett.* **4**, 1770–1777 (2019).
38. Subramanian, S. et al. Geometric catalyst utilization in zero-gap CO<sub>2</sub> electrolyzers. *ACS Energy Lett.* **8**, 222–229 (2023).
39. Tanner, C. C. The Soret effect. *Nature* **170**, 34–35 (1952).
40. Monisha, K., Suresh, K. & George, S. D. Colloidal manipulation through plasmonic and non-plasmonic laser-assisted heating. *Laser Photonics Rev.* **17**, 2300303 (2023).
41. Mentor, J. J. et al. The Soret effect in dry polymer electrolyte. *Mol. Syst. Des. Eng.* **5**, 856–863 (2020).
42. Kutz, R. B. et al. Sustainion imidazolium-functionalized polymers for carbon dioxide electrolysis. *Energy Technol.* **5**, 929–936 (2017).
43. Leaist, D. G. & Hui, L. Conductometric determination of the soret coefficients of a ternary mixed electrolyte. reversed thermal diffusion of sodium chloride in aqueous sodium hydroxide solutions. *J. Phys. Chem.* **94**, 447–451 (1990).
44. Moore, R. C., Mesmer, R. E. & Simonson, J. M. Solubility of potassium carbonate in water between 384 and 529 K measured using the synthetic method. *J. Chem. Eng. Data* **42**, 1078–1081 (1997).
45. Lee, W. H. et al. Highly selective and stackable electrode design for gaseous CO<sub>2</sub> electroreduction to ethylene in a zero-gap configuration. *Nano Energy* **84**, 105859 (2021).
46. Zhang, X. Y. et al. In operando identification of in situ formed metalloid Zinc $\delta$ <sup>+</sup> active sites for highly efficient electrocatalyzed carbon dioxide reduction. *Angew. Chem. Int. Ed.* **61**, 1–9 (2022).
47. Ren, S. et al. Molecular electrocatalysts can mediate fast, selective CO<sub>2</sub> reduction in a flow cell. *Science* **365**, 367–369 (2019).
48. Kong, S. et al. Delocalization state-induced selective bond breaking for efficient methanol electrosynthesis from CO<sub>2</sub>. *Nat. Catal.* **6**, 6–15 (2023).
49. Ye, K. et al. Resolving local reaction environment toward an optimized CO<sub>2</sub>-to-CO conversion performance. *Energy Environ. Sci.* **15**, 749–759 (2022).
50. Wen, G. et al. Continuous CO<sub>2</sub> electrolysis using a CO<sub>2</sub> exsolution-induced flow cell. *Nat. Energy* **7**, 978–988 (2022).
51. Abraham, E. et al. Highly transparent silanized cellulose aerogels for boosting energy efficiency of glazing in buildings. *Nat. Energy* **8**, 381–396 (2023).
52. Smith, T. J. & Stevenson, K. J. *4-Reference Electrodes. Handbook of Electrochemistry* <https://doi.org/10.1016/B978-0-444-51958-0.50005-7> (Elsevier B.V., 2007).
53. Longhi, P., Mussini, T., Orsenigo, R. & Rondinini, S. Redetermination of the standard potential of the mercuric oxide electrode at temperatures between 283 and 363 K and the solubility product constant of mercuric hydroxide. *J. Appl. Electrochem.* **17**, 505–514 (1987).
54. McCrory, C. C. L., Jung, S., Peters, J. C. & Jaramillo, T. F. Benchmarking heterogeneous electrocatalysts for the oxygen evolution reaction. *J. Am. Chem. Soc.* **135**, 16977–16987 (2013).
55. Solubility of Gases in Water vs. Temperature. [www.engineeringtoolbox.com](http://engineeringtoolbox.com) (2024).
56. Duan, Z. & Sun, R. An improved model calculating CO<sub>2</sub> solubility in pure water and aqueous NaCl solutions from 273 to 533 K and from 0 to 2000 bar. *Chem. Geol.* **193**, 257–271 (2003).

## Acknowledgements

The authors acknowledge the National Natural Science Foundation of China under Grant No. 52376191. The Shenzhen Science and Technology Innovation Commission under Grant 20231120185819001 and KCXST2022102111207017, the Guangdong Basic and Applied Basic Research Foundation under Grant No. 2023A1515011595, Guangdong Major Project of Basic and Applied Basic Research (2023B0303000002), and Guangdong grant under Grant No. 2021QN02L562 are also acknowledged for their support. The computation in this work is supported by the Center for Computational Science and Engineering at Southern University of Science and Technology.

## Author contributions

M.L. conceived and supervised the study. J.L. contributed to the conceptualization of the study and experiment design. H.Z. performed the simulation. J.L., C.L., and W.X. contributed to the material characterization, electrochemical experiments, and data analysis. D.C. contributed to the Soret coefficient test. J.L. wrote the original manuscript draft, and all authors participated in critical revision and final approval of the paper.

## Competing interests

The authors declare no competing interests.

## Additional information

**Supplementary information** The online version contains supplementary material available at <https://doi.org/10.1038/s41467-025-59604-6>.

**Correspondence** and requests for materials should be addressed to Meng Lin.

**Peer review information** *Nature Communications* thanks the anonymous, reviewer(s) for their contribution to the peer review of this work. A peer review file is available.

**Reprints and permissions information** is available at <http://www.nature.com/reprints>

**Publisher's note** Springer Nature remains neutral with regard to jurisdictional claims in published maps and institutional affiliations.

**Open Access** This article is licensed under a Creative Commons Attribution-NonCommercial-NoDerivatives 4.0 International License, which permits any non-commercial use, sharing, distribution and reproduction in any medium or format, as long as you give appropriate credit to the original author(s) and the source, provide a link to the Creative Commons licence, and indicate if you modified the licensed material. You do not have permission under this licence to share adapted material derived from this article or parts of it. The images or other third party material in this article are included in the article's Creative Commons licence, unless indicated otherwise in a credit line to the material. If material is not included in the article's Creative Commons licence and your intended use is not permitted by statutory regulation or exceeds the permitted use, you will need to obtain permission directly from the copyright holder. To view a copy of this licence, visit <http://creativecommons.org/licenses/by-nc-nd/4.0/>.

© The Author(s) 2025